The Thesis Committee for Hyunbae Park
Certifies that this is the approved version of the following thesis :

The Kinetic Sunyaev-Zel'dovich effect as a probe of the physics of cosmic reionization: the effect of self-regulated reionization

APPROVED BY

SUPERVISING COMMITTEE:

Supervisor:

Paul R. Shapiro

Milos Milosavljevic

The Kinetic Sunyaev-Zel'dovich effect as a probe of the physics of cosmic reionization: the effect of self-regulated reionization

by

Hyunbae Park, B.S.

THESIS

Presented to the Faculty of the Graduate School of

The University of Texas at Austin

in Partial Fulfillment

of the Requirements

for the Degree of

MASTER OF ARTS

THE UNIVERSITY OF TEXAS AT AUSTIN

December 2014

Acknowledgments

The Kinetic Sunyaev-Zel'dovich effect as a probe of the physics of cosmic reionization: the effect of self-regulated reionization

Hyunbae Park, M.A.

The University of Texas at Austin, 2014

Supervisor: Paul R. Shapiro

We calculate the angular power spectrum of the Cosmic Microwave Background (CMB) temperature fluctuations induced by the kinetic Sunyaev-Zel'dovich (kSZ) effect from the epoch of reionization (EOR). We use detailed N-body+radiative transfer simulations to follow inhomogeneous reionization of the intergalactic medium (IGM). For the first time we take into account the "self-regulation" of reionization: star formation in low-mass dwarf galaxies ($10^8 \ M_\odot \lesssim M \lesssim 10^9 \ M_\odot$) or minihalos ($10^5 \ M_\odot \lesssim M \lesssim 10^8 \ M_\odot$) is suppressed if these halos form in the regions that were already ionized or Lyman-Werner dissociated. Some previous work suggested that the amplitude of the kSZ power spectrum from the EOR can be described by a two-parameter family: the epoch of half ionization and the duration of reionization. However, we argue that this picture applies only to simple forms of the reionization history which are roughly symmetric about the half-ionization epoch. In self-regulated reionization, the universe begins to be ionized early, maintains a

low level of ionization for an extended period, and then finishes reionization as soon as high-mass atomically-cooling halos dominate. While inclusion of self-regulation affects the amplitude of the kSZ power spectrum only modestly ($\sim 10\%$), it can change the duration of reionization by a factor of more than two. We conclude that the simple two-parameter family does not capture the effect of a physical, yet complex, reionization history caused by self-regulation. When added to the post-reionization kSZ contribution, our prediction for the total kSZ power spectrum is below the current upper bound from the South Pole Telescope. Therefore, the current upper bound on the kSZ effect from the EOR is consistent with our understanding of the physics of reionization.

Table of Contents

List of Tables

List of Figures

Chapter 1

Introduction

How was the intergalactic medium (IGM) reionized before $z = 6$? The secondary anisotropy of the cosmic microwave background (CMB) at $l > 3000$ allows us to probe the physics of cosmic reionization via the kinetic Sunyaev-Zel'dovich (kSZ) effect [30]. The temperature of the CMB changes as free electrons in ionized gas Compton scatter CMB photons: the bulk peculiar velocity of electrons induces Doppler shifts in the energy of the CMB photons. While the spectrum of the CMB remains that of a black body, its temperature changes.[2]

Inhomogeneity in the density and velocity of electrons, as well as inhomogeneity in ionization fraction, will induce temperature fluctuations in the

---

[1]The main contents of this thesis have been published as [22]. Among the co-authors of [22], Paul R. Shapiro and Eiichiro Komatsu contributed to the project by adivsing the author and Ilian T. Iliev, Garrelt Mellema and Kyungjin Ahn generated and provided the scientific data used in the work.

[2]A related effect results from the thermal motions of free electrons in the hot intracluster gas, called the thermal SZ effect (tSZ). Multiwavelength observations allow a distinction between the kSZ and tSZ effects on the CMB. Here, we shall focus on the kSZ signal alone.

CMB, $\Delta T/T$, given by

$$\frac{\Delta T(\hat{\gamma})}{T} = -\int d\tau e^{-\tau} \frac{\hat{\gamma} \cdot \mathbf{v}}{c}, \tag{1.1}$$

where $\hat{\gamma}$ is the line-of-sight unit vector, $\mathbf{v}$ the peculiar velocity field, and τ the optical depth to Thomson scattering integrated through the IGM from $z = 0$ to the surface of last scattering at $z_{\mathrm{rec}} \approx 10^3$, where

$$d\tau = c \; n_e(z)\sigma_{\mathrm{T}}(\frac{dt}{dz})dz. \tag{1.2}$$

There are two contributions to the kSZ signal:

1. **Post-reionization contribution**. This is the contribution from redshifts below $z = z_{\mathrm{ov}}$, where z_{ov} is the redshift at which reionization is finished, when individual H II bubbles fully overlap with one another. While the post-reionization contribution depends upon the value of z_{ov}, for which quasar absorption spectra suggest $z_{\mathrm{ov}} \sim 6 - 7$, it is not too sensitive to the exact value of z_{ov}. We shall not discuss this contribution in this paper, but discuss it in a subsequent paper (Park et al., in preparation).

2. **Reionization contribution**. This is the contribution from redshifts above $z = z_{\mathrm{ov}}$, where the ionization was patchy and incomplete. This contribution depends not only on z_{ov}, but also on the details of the time and spatial variation of inhomogeneous reionization, which are not yet well constrained; thus, we must explore how predictions vary for different

2

models of reionization. The reionization contribution is the main focus of this paper.

Modeling the reionization contribution is a challenge, as the universe was not ionized homogeneously, but in patches. These patches grow over time until they overlap, finishing reionization of the universe. The distribution of these patches is determined by non-linear physics: non-linear clustering of the sources of ionizing photons; non-linear clumping of gas in the IGM; and complex morphologies of patches resulting from propagation of ionization fronts in the clumpy IGM. Accurately calculating the reionization contribution thus requires numerical simulations of cosmological structure formation coupled with radiative transfer.

To model the formation and spatial clustering of the sources of ionizing photons, cosmological simulations must be performed in a volume large enough to capture the crucial spatial variations of this process in a statistically meaningful way. This requires a volume greater than ~ 100 comoving Mpc across, because H II bubbles can typically grow as large as ~ 20 comoving Mpc in size. These simulations must also have a high enough mass resolution to resolve the formation of the individual galaxies which are the sources of ionizing radiation; thus, billions of particles are required. The radiative transfer of ionizing photons is then calculated on the IGM density and velocity fields computed by the cosmological simulation.

What do current observational data tell us? The South Pole Telescope

3

(SPT) experiment has detected an excess temperature anisotropy for the CMB on small angular scales, which they attribute to the SZ effect. By subtracting the dominant contribution from the tSZ effect by using multiwavelength observations to distinguish it from the kSZ effect, the SPT detection yields an upper limit to the total kSZ contribution. The measurements are usually reported in terms of the angular power spectrum, $C_l \equiv \frac{1}{2l+1} \sum_m |a_{lm}|^2$. Here, $a_{lm} \equiv \int d^2\hat{\gamma} \Delta T(\hat{\gamma}) Y_{lm}^*(\hat{\gamma})$ is the coefficient of spherical-harmonics mode, Y_{lm}, of ΔT. The SPT collaboration reports their measurements in terms of the quantity

$$D_l \equiv \frac{l(l+1)C_l}{2\pi}, \tag{1.3}$$

which we shall compute in this paper. SPT has placed an upper bound on the kSZ D_l at $l = 3000$ of $D_{l=3000}^{\mathrm{kSZ}} < 2.8\ \mu K^2$ [24]. The detection of the total SZ effect is complicated by the possible contamination of the fluctuating signal caused by the cosmic infrared background (CIB) from individual galaxies. The kSZ limit loosens to 6.7 μK^2 when allowance is made for a possible correlation between the thermal Sunyaev-Zel'dovich effect (tSZ) [37] and the CIB. [3]Our goal is to see whether these current upper bounds are consistent with our models of reionization.

---

[3]After our paper was written, a new paper was posted with SZ results from the Atacama Cosmology Telescope (ACT) [5]. These new results have higher uncertainty than those quoted above from SPT, but when they are combined with those of SPT and allowance is made for a more limited tSZ-CIB correlation than that allowed by [24], the ACT+SPT kSZ upper limit quoted by [5] is 5.0 μK^2 (i.e. between the SPT values with and without tSZ-CIB correlation, of 6.7 μK^2 and 2.8 μK^2, respectively). Recently, [4] refined their separation of the tSZ and kSZ contribution to the total SZ power spectrum by using the tSZ bispectrum to derive the tSZ power spectrum. With allowance for tSZ-CIB correlation, they now report $D_{l=3000}^{\mathrm{kSZ}} = 2.9 \pm 1.5\ \mu K^2$ (1σ error bars), or a 95% confidence upper limit of 5.5 μK^2.

Following the early analytical calculation done by Vishniac for linear density and velocity perturbations in a fully ionized medium [16, 32], calculations of the kSZ effect by cosmic reionization have steadily improved over time. Further analytical calculations later incorporated the effects of inhomogeneous reionization in an approximate manner [9, 26]. A "semi-numerical" approach was also developed by combining the simulated density and velocity fields from N-body simulations with an analytical ansatz for tracking the reionization process [19, 36].

Early, pioneering calculations using structure formation simulations coupled with radiative transfer to model inhomogeneous reionization numerically [8, 25] underestimated the amplitude of the kSZ signal, as they used computational boxes too small to capture the impact of large-scale velocity modes and H II bubbles or an accurate measure of the duration of the global EOR. This was demonstrated by the first calculations of reionization based on truly large-scale (> 100 Mpc) radiative transfer simulations, which resolved the formation of all galactic halo sources above $2 \times 10^9 \ M_\odot$ [11, 14]. These later simulations demonstrated the importance of a large enough simulation volume to capture the effects of long-wavelength fluctuations properly. They were also the first to realize that it is necessary to correct the kSZ power spectrum for the missing velocity power due to the finite box size of the simulations.

For the mass range of galactic halos resolved by these simulations, $\gtrsim 10^9 \ M_\odot$, stars – the *sources* of reionization – were able to form when the primordial composition gas inside the halos cooled radiatively by atomic pro-

cesses involving H atoms. They are known as "atomic cooling halos" to distinguish them from minihalos of mass $M \lesssim 10^8 \ M_\odot$, with virial temperature $T_{\mathrm{vir}} \lesssim 10^4 K$, for which star formation is possible only if H_2 molecules form in sufficient abundance to cool the gas below T_{vir} by rotational-vibrational line excitation. Atomic-cooling halos with $10^8 \ M_\odot \lesssim M \lesssim 10^9 \ M_\odot$ also exist and are even more abundant than those with $M \gtrsim 10^9 \ M_\odot$. These low-mass atomic-cooling halos ("LMACHs"), however, are prevented from forming stars if they form within an ionized patch of the IGM, where the gas pressure of the photoheated IGM opposes the accretion of baryons onto these halos. This "self-regulates" their contribution to reionization as the global ionized fraction grows with time and more and more of these halos are born within the ionized zones [12, 27]. While the precise value of halo mass which defines the upper edge of this "Jeans-filtered" mass-range is still uncertain, the high-mass atomic-cooling halos ("HMACHs") above $\sim 10^9 \ M_\odot$ are generally free of this suppression.

To simulate the impact of both LMACHs and HMACHs on reionization, it was necessary for [12] to increase their halo mass resolution so as to resolve all the LMACHs, too, by reducing the simulation box size to 53 Mpc on a side at fixed N-body particle number. This led to the first radiative transfer simulations of "self-regulated" reionization, which demonstrated the importance of including and then suppressing the LMACHs to start reionization earlier and extend its duration [12]. While the end of reionization is still set by the rapid rise of the HMACHs, in that case, when they eventually

surpass the saturated contribution of the suppressible LMACHs, the effect of the LMACHs is to boost the electron-scattering optical depth, τ, integrated through the EOR. Such an effect can be important for the kSZ fluctuations from the EOR, too, but simulating this required us to increase the simulation volume again while retaining the high mass resolution required to resolve the LMACHs, too.

Our next generation of simulations involved boxes 163 Mpc on a side, a volume large enough to predict observables like the kSZ effect, but with N-body simulations large enough to resolve all halos down to 10^8 $M_\odot$ and incorporate ionization suppression ("Jeans-filtering") of the halos of mass between 10^8 $M_\odot$ and 10^9 $M_\odot$ [13]. These smaller-mass halos (LMACHs) are more abundant and likely to be more efficient ionizing sources, as they may have higher escape fraction and emissivity [13]. However, as described above, they may be suppressed as sources if they form inside ionized regions, where ionization heats the gas and makes its pressure high enough to resist gravitational collapse into such small galaxies. Recently, an additional simulation was performed, including this new physics, in an even larger volume (~ 600 Mpc) (Iliev et al. in preparation).

[1] expanded the mass range even further by accounting for starlight emitted by minihalos ($10^5 - 10^8$ $M_\odot$), as well. In addition to their Jeans-mass filtering in ionized regions, they may also be suppressed if molecular hydrogen in minihalos is photo-dissociated by Lyman-Werner band photons in the UV background below 13.6 eV also emitted by the sources of reionization. We

7

thus have a simulated model which takes into account all the halos down to 10^5 $M_\odot$ as sources of reionization.

It is important now to determine if and how the kSZ fluctuations from the epoch of reionization are different from the previous predictions when this "self-regulated" reionization is taken into account. That is the prime focus of this paper. Some of our results were first summarized in [28].

Recently, [21], [35] and [2] compared the predicted kSZ power spectra from their semi-numerical calculations, to the upper bounds from the SPT data [24], obtaining limits on the epoch and the duration of the reionization. Those studies concluded that, for a given value of the total Thomson-scattering optical depth, the reionization contribution to the kSZ signal is mostly sensitive to the duration of the reionization defined as $\Delta z \equiv z_{99\%} - z_{20\%}$ [35] or $z_{75\%} - z_{25\%}$ [2, 21]. [35] claim that the upper bound on $D^{\mathrm{kSZ}}_{l=3000}$ from the SPT data implies $\Delta z < 4$ (95% CL) for no tSZ-CIB correlation, and $\Delta z < 7$ (95% CL) for the maximum possible tSZ-CIB correlation. However, as their methods are based on an analytical ansatz for the reionization process, it is necessary to use more self-consistent calculations of radiative transfer such as our simulation results to revisit this issue. We note that [34] compared their semi-numerical approach to their own numerical simulations using radiative transfer, finding an agreement at the level of 50%.

The remainder of this paper is organized as follows. In Section 2, we express the kSZ power spectrum in terms of a line-of-sight integral of the transverse momentum power spectrum, and show how the transverse momentum

8

power spectrum is related to the statistics of the density and velocity fields of ionized gas. In Section 3, we describe the details of the simulations used for our study. In Section 4, we present our predictions for the kSZ power spectrum and discuss the effects of inhomogeneous reionization as well as of self-regulated reionization. In Section 5, we compare our results with the recent semi-numerical calculations, and show that inclusion of self-regulated reionization qualitatively changes the parameter dependence of the kSZ power spectrum from that without self-regulation. In Section 6, we summarize our conclusions. In Appendix A, we give the derivation of the kSZ power spectrum written in terms of the transverse momentum power spectrum. In Appendix B, we show how to correct for the missing power due to a finite box size of simulations in our method.

Chapter 2

Basics

2.1 Angular power spectrum of the kSZ effect

As the Thomson-scattering optical depth, τ, is proportional to the free electron number density, the kSZ effect given by Equation (1.1) depends mainly on the *specific ionized momentum* field of the ionized medium,

$$\mathbf{q} \equiv \chi \mathbf{v}(1 + \delta), \tag{2.1}$$

henceforth referred to only as "momentum". Here, $\chi \equiv n_e/(n_{\mathrm{H}} + 2n_{\mathrm{He}})$ is the ionization fraction, and $\delta \equiv (\rho - \bar{\rho})/\bar{\rho}$ is the density contrast of baryons. In general, the baryon density is different from the dark matter density, especially on scales smaller than the Jeans length. In this paper, we shall assume that baryons trace dark matter particles, as we are interested in scales bigger than the Jeans length of gas at 10^4 K.

We rewrite Equation (1.1) using $\mathbf{q}$ as

$$\frac{\Delta T}{T}(\hat{\gamma}) = -\frac{\sigma_T \bar{n}_{e,0}}{c} \int \frac{ds}{a^2} \, e^{-\tau} \mathbf{q} \cdot \hat{\gamma}. \tag{2.2}$$

Here, σ_T is the Thomson scattering cross section, $\bar{n}_{e,0} = \bar{n}_{\mathrm{H},0} + 2\bar{n}_{\mathrm{He},0}$, is the mean number density of electrons at the (fully-ionized) present epoch, and s

is the distance travelled by photons from a source to the observer in comoving units.

The kSZ angular power spectrum is given by[1] [See Appendix A for derivation; also see [18], but note that their Equation (4) contains a typo: it is off by a factor of $(c/H_0)^2$]:

$$C_l = \left(\frac{\sigma_T \bar{n}_{e,0}}{c}\right)^2 \int \frac{ds}{s^2 a^4} e^{-2\tau} \frac{P_{q_\perp}(k = l/s, s)}{2}, \qquad (2.3)$$

where $\tilde{\mathbf{q}}_\perp(\mathbf{k}) = \tilde{\mathbf{q}}(\mathbf{k}) - \hat{k}[\tilde{\mathbf{q}}(\mathbf{k}) \cdot \hat{k}]$ is the projection of $\tilde{\mathbf{q}}(\mathbf{k}) \equiv \int d^3\mathbf{x} \, e^{i\mathbf{k}\cdot\mathbf{x}}\mathbf{q}(\mathbf{x})$ on the plane perpendicular to the mode vector $\mathbf{k}$ (i.e., $\tilde{\mathbf{q}}_\perp \cdot \mathbf{k} = 0$), $\hat{k} \equiv \mathbf{k}/|\mathbf{k}|$ is a unit vector, and $P_{q_\perp}$ is the power spectrum of $\tilde{\mathbf{q}}_\perp$ defined by $(2\pi)^3 P_{q_\perp}(k)\delta^D(\mathbf{k} - \mathbf{k}') \equiv \langle \tilde{\mathbf{q}}_\perp(\mathbf{k}) \cdot \tilde{\mathbf{q}}_\perp^*(\mathbf{k}') \rangle$. Note that $\tilde{\mathbf{q}}_\perp$ is often called a transverse (or curl) mode. A longitudinal (or gradient) mode is parallel to $\mathbf{k}$ and is given by $\tilde{\mathbf{q}}_\parallel(\mathbf{k}) = \hat{k}[\tilde{\mathbf{q}}(\mathbf{k}) \cdot \hat{k}]$.

As we show in Appendix A, in the small-angle approximation, the line-of-sight integral cancels out the contribution from $\tilde{\mathbf{q}}_\parallel$ and a half of the power of $\tilde{\mathbf{q}}_\perp$, leaving only the remaining half of $P_{q_\perp}$. This explains a factor of two in the denominator of Equation (2.3).

Helium atoms are assumed to be singly ionized where hydrogen atoms

---

[1]All previous numerical calculations of the kSZ power spectrum first created maps using Equation (2.2) and then measured C_l from the two-dimensional Fourier transform of the simulated maps. In this paper, we shall use Equation (2.3) to compute C_l using $P_{q_\perp}$ measured from three-dimensional simulation boxes at various redshifts, without ever creating maps. While we are the first to apply this method to the computation of the kSZ power spectrum, this method has been applied successfully to the computation of the tSZ power spectrum [23] as well as to that of the power spectrum of anisotropy of the near infrared background [6, 7].

are ionized at least until $z_{\rm ov}$, the redshift which all the H II bubbles overlap to finish the ionization of hydrogen atoms due to the similar ionization potential of H I and He I. Helium atoms remain singly ionized until much later, $z \approx 3$, after which they are thought to be doubly ionized. As we are interested only in the epoch of hydrogen-reionization, $z \gtrsim 6$, we shall assume that the ionized fraction, χ, is given by $\chi = (0.92)X$, where X is the hydrogen ionized fraction at each point in our radiative transfer simulation: χ saturates at 0.92 in fully ionized regions during hydrogen reionization, as 8% of the electrons are left bound in singly-ionized helium atoms.

2.2 Power spectrum of the curl of the momentum

Table 2.1: Reionization simulation parameters and global reionization history results

Label	Sources	$g_{\gamma,\rm H}$ $(f_{\gamma,\rm H})$	$g_{\gamma,\rm L}$ $(f_{\gamma,\rm L})$	$g_{\gamma,\rm MH}$ $(f_{\gamma,\rm MH})$	$\tau_{\rm es}$	$z_{10\%}$	$z_{90\%}$	$z_{\rm ov}$
L1	HMACHs+LMACHs	8.7(10)	130(150)	-	0.080	13.3	8.6	8.3
L2(XL2)	HMACHs+LMACHs	1.7(2)	8.7(10)	-	0.058	9.9	6.9	6.8
L2M1J1	HMACHs+LMACHs+MHs	1.7(2)	8.7(10)	5063(1030)	0.086	17.4	6.9	6.8
L3	HMACHs only	21.7(25)	-	-	0.070	10.3	9.1	8.4

Our goal is to compute the power spectrum of the curl of the momentum field, $P_{q_\perp}$, and evaluate Equation (2.3) to obtain C_l.

Assuming that the velocity field stays longitudinal, i.e., parallel to $\mathbf{k}$, $P_{q_\perp}$ is given by the second-order term in the momentum: $\mathbf{q}_\perp = (\int \frac{d^3 k'}{(2\pi)^3} \delta(\mathbf{k} - \mathbf{k}')\mathbf{v}(\mathbf{k}'))_\perp$. This assumption is exact in the linear regime and is approximately

true in the non-linear regime, as this second-order term dominates in the non-linear regime anyway. This gives [18]

$$P_{q_\perp}(k, z) = \int \frac{d^3k'}{(2\pi)^3}(1 - \mu'^2)\left[P_{\delta\delta}(|\mathbf{k} - \mathbf{k}'|)P_{vv}(k')\right.$$
$$\left. - \frac{k'}{|\mathbf{k} - \mathbf{k}'|}P_{\delta v}(|\mathbf{k} - \mathbf{k}'|)P_{\delta v}(k')\right], \quad (2.4)$$

where $\mu' \equiv \hat{k} \cdot \hat{k}'$. Here, $P_{\delta\delta}P_{vv}$ term gives a positive contribution, whereas $P_{\delta v}P_{\delta v}$ term gives a negative contribution from the density field correlated with the velocity field that does not have a curl component.

Due to a finite box size of simulations, we must correct for the missing velocity power coming from modes whose wavelength is longer than the size of the simulation box [14]. We shall describe our correction method in Appendix B.

At high redshift where the density and velocity fields are still in the linear regime, the velocity power spectrum is related to the linear density power spectrum by $P_{vv}(k) = (\dot{a}f/k)^2 P_{\delta\delta}^{\text{lin}}(k)$, where $f \equiv d\ln\delta/d\ln a$ and $a(t)$ is the Robertson-Walker scale factor. This gives the so-called Ostriker-Vishniac (OV) spectrum [32]:

$$P_{q_\perp}^{\text{OV}}(k, z) = \dot{a}^2 f^2 \int \frac{d^3k'}{(2\pi)^3}P_{\delta\delta}^{\text{lin}}(|\mathbf{k} - \mathbf{k}'|, z)P_{\delta\delta}^{\text{lin}}(k', z)$$
$$\times \frac{k(k - 2k'\mu')(1 - \mu'^2)}{k'^2(k^2 + k' - 2kk'\mu')}. \quad (2.5)$$

The OV spectrum provides a useful check of the numerical simulation and the way we correct for the missing velocity. In the left panel of Figure 2.1, we show

13

an excellent agreement between the OV spectrum and the simulation result at $z = 9$, after correcting for the missing velocity power due to a finite box size of the simulation.

Finally, one can incorporate the effect of inhomogeneous reionization into the equation by replacing δ in Equation (2.4) by $\chi(1 + \delta)$:

$$
\begin{aligned}
P_{q_\perp}&(k, z) \\
&= \int \frac{d^3 k'}{(2\pi)^3} (1 - \mu'^2) \Big[P_{\chi(1+\delta),\chi(1+\delta)}(|\mathbf{k} - \mathbf{k}'|) P_{vv}(k') \\
&\qquad - \frac{k'}{|\mathbf{k} - \mathbf{k}'|} P_{\chi(1+\delta),v}(|\mathbf{k} - \mathbf{k}'|) P_{\chi(1+\delta),v}(k') \Big].
\end{aligned}
\tag{2.6}
$$

Note that we do *not* use this equation to compute $P_{q_\perp}$, but compute $P_{q_\perp}$ directly from the simulation. However, we use this equation to estimate and correct for the missing power due to a finite box size of the simulation as described in Appendix B. We then use the corrected $P_{q_\perp}$ in Equation (2.3) to compute the angular power spectrum. As shown in the right panel of Figure 2.1, the effect of reionization inhomogeneity substantially boosts the power spectrum relative to the homogeneously-ionized case, while correcting for the missing velocity power of the finite simulation volume boosts it even further.

14
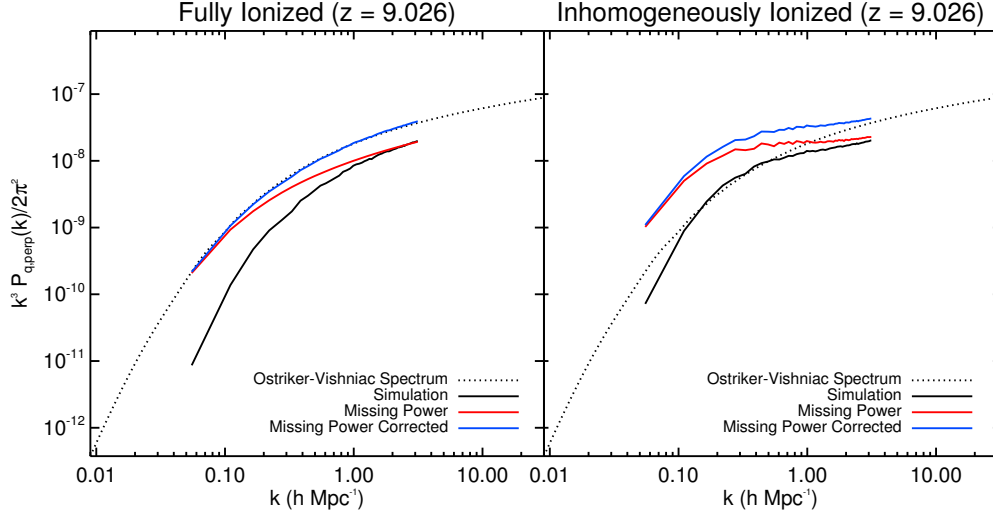
Figure 2.1: Dimensionless power spectra of the curl of the momentum field, $k^3 P_{q_\perp}(k)/(2\pi^2)$, at $z = 9$ calculated from the simulation with 114 h^{-1} Mpc in a side. The black solid lines show the raw power spectrum obtained from the N-body simulation, while the blue lines show the power spectrum after corrected being for the missing velocity power due to a finite box size of the simulation. The red lines show the missing power added to the black solid lines. The dotted lines show the analytical OV spectrum given in Equation (2.5). Left: fully ionized case. An excellent agreement between the OV spectrum and the corrected power spectrum shows the validity of our simulation as well as that of our method to correct for the missing velocity power. Right: inhomogeneously ionized case, L3. The power spectrum is significantly enhanced at $k \lesssim 1$ h Mpc^{-1}.

Chapter 3

Reionization Simulation

3.1 Basic simulation parameters

The simulations that we shall use in this paper consist of two parts: (1) cosmological N-body simulations of collisionless particles using the "CubeP^{3}M" N-body code [10]; and (2) radiative-transfer of H-ionizing photons in the density and source fields created from this N-body simulation results using the "C^2-Ray" (Conservative, Causal Ray-tracing) code [20]. The details of the simulations that we shall use in this paper are described in [13] and [1].

Unless specified otherwise, the reionization simulations are run on the density and source fields from the same N-body results with 3072^3 particles in a comoving box of 114 h^{-1} Mpc on a side. Halos are identified down to 10^8 $M_\odot$ with at least 20 particles, using a spherical overdensity halo finder with overdensity of 178 times the mean cosmic density. One of the models uses another N-body simulation with a larger box of 425 h^{-1} Mpc, with 5488^3 particles, resolving halos down to 10^9 $M_\odot$. The background cosmology is based on the *WMAP* 5-year data combined with constraints from baryonic acoustic oscillations and high-redshift Type Ia supernovae ($\Omega_M = 0.27, \Omega_\Lambda = 0.73, h = 0.7, \Omega_b = 0.044, \sigma_8 = 0.8, n_s = 0.96$; [17]).

For the 114 h^{-1} Mpc, we then calculate the IGM density field from the particle data with halos excluded adaptively-smoothed on to a 256^3 radiative-transfer grid in order to generate ionization maps using the C^2-Ray code. Therefore, the final physical length resolution of the reionization models is $d_{\text{cell}} = 0.45 \; h^{-1}$ Mpc. The highest l-mode that we can calculate from the simulation is given by $l_{\text{limit}} = k_{\text{Nyq}}s(z_{\text{ov}})$, where $k_{\text{Nyq}} = \pi/(2d_{\text{cell}})$ is the Nyquist frequency, and $s(z_{\text{ov}})$ is the comoving distance out to the end of reionization. For example, $z_{\text{ov}} = 6.6$ gives $l_{\text{limit}} = 22000$.

The new simulations also incorporate the effects of even smaller halos in $10^5 \; M_\odot < M < 10^8 \; M_\odot$, using a sub-grid prescription calibrated by smaller-box N-body simulations with higher-resolution having 1728^3 particles in a box of 6.3 h^{-1} Mpc [1]. Specifically, we find that there is a correlation between the number of these small-mass halos in each cell and the total matter density averaged over that cell, with cells of size 0.45 h^{-1} Mpc, which coincides with the size of the radiative transfer cells in our 114 h^{-1} Mpc C^2-ray simulations. We then use this correlation to calculate the number of small-mass halos in each of the radiative-transfer cells in our 114 h^{-1} Mpc simulations.

For our most recent simulation, in a box 425 h^{-1} Mpc on a side, the RT grid has 504^3 cells, so $d_{\text{cell}} = 0.84 \; h^{-1}$ Mpc, slightly larger than that for the other simulations, and $l_{\text{limit}} \sim 12000$. In this larger-box simulation, low-mass halos between 10^8 and $10^9 \; M_\odot$ are included by a subgrid model like that described above for MHs.

3.2   Varying physics of reionization

What kind of sources are responsible for reionization? In this section, we consider a set of reionization simulations based on source models of increasing sophistication from the one with only high-mass sources to the one with all kinds of sources down to least massive halos in our models.

For each halo identified in our simulation, we calculate the number of ionizing photons which escape from it into the IGM per unit time, $\dot{N}_\gamma$, which is assumed to be proportional to the halo mass, M:

$$\dot{N}_\gamma = \frac{f_\gamma M \Omega_b}{\Delta t \, \Omega_0 m_p} \, , \tag{3.1}$$

where m_p is the proton mass, Δt is the duration of each star-forming episode (i.e. which corresponds in practice to the radiative transfer simulation time-step), and $f_\gamma = f_{\rm esc} f_\star N_\star$ is the number of ionizing photons produced and released by the halo over the lifetime of the stars which form inside it in this time step, per halo atom, if f_* is the fraction of the halo atoms which form stars during this burst, $f_{\rm esc}$ is the fraction of the ionizing photons produced by these stars which escapes into the IGM and the integrated number of ionizing photons released over their lifetime per stellar atom is given by $N_\star$. The latter parameter depends on the assumed IMF for the stellar population and can range from $\sim 4,000$ (e.g. for Pop II stars with a Salpeter IMF) to $\sim 100,000$ (e.g. for a top-heavy IMF of Pop III stars). Halos were assigned different efficiencies according to their mass, grouped according to whether their mass was above ("HMACHs") or below ("LMACHs") $10^9 M_\odot$ (but above $10^8 M_\odot$, the

minimum resolved halo mass). Low-mass sources are assumed to be suppressed within ionized regions (for ionization fraction higher than 10%), through Jeans-mass filtering, as discussed in [12].

In addition to the source efficiency parameter, f_γ, we also define a slightly different factor, g_γ, that is given by

$$g_\gamma = f_\gamma \left(\frac{10 \text{ Myr}}{\Delta t} \right) \quad (3.2)$$

where Δt is the time between two snapshots from the N-body simulation. The new factor g_γ reflects the fact that a given halo has a luminosity which depends on the ratio of f_γ to Δt, so g_γ has the advantage that it is independent of the length of the time interval between the density slices, and as such it allows a direct comparison between runs with different Δt. For the reader's convenience, we listed the values of both parameters in Table 2.1. The specific numerical values of the efficiency parameters are strongly dependent on the background cosmology adopted and the minimum source halo mass. Therefore, parameter values for simulations based on different underlying cosmology and halo mass resolution should not be compared directly, but require cosmology and resolution-dependent conversion coefficients to achieve the same reionization history.

3.2.1 HMACHs-only model

In our simplest model (labeled as L3; see Table 2.1 for the details. Note that "L" stands for a "large volume"), we only use HMACHs as the sources of
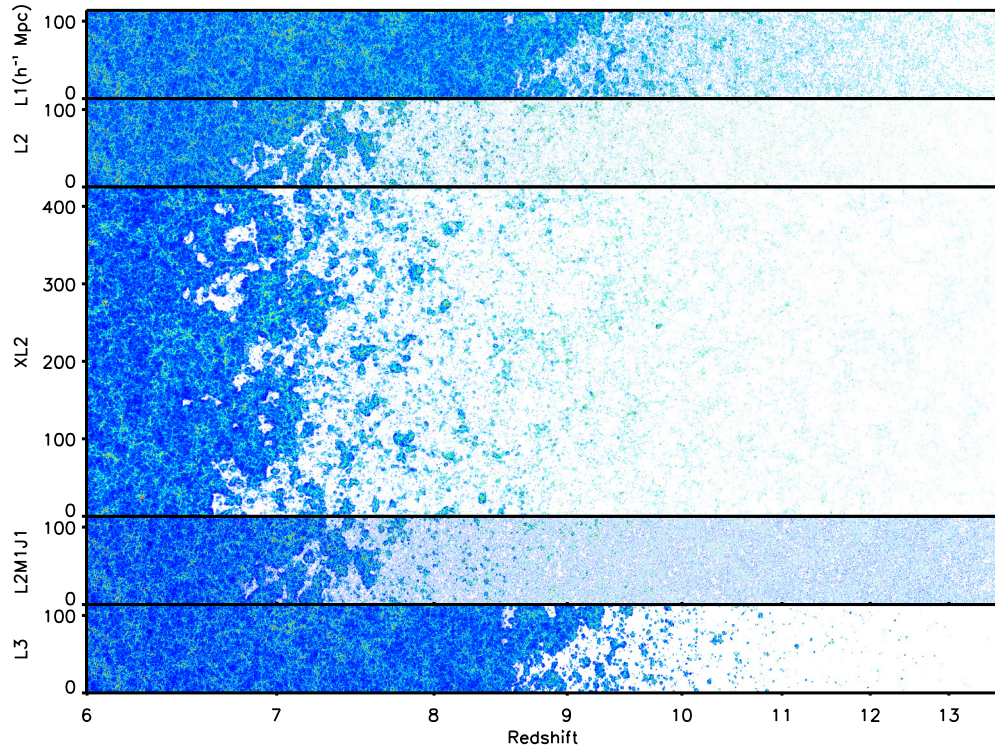
Figure 3.1: Cuts through the N-body+Radiative Transfer simulations used in this work. See Table 2.1 for the parameters of models L1, L2, L2M1J1, and L3. While these runs have the box size of 114 h^{-1} Mpc, the model XL2 has the box size of 425 h^{-1} Mpc and has the same model parameters as the model L2. Each panel shows the matter density distribution *multiplied by spatially-varying ionization fractions*. For example, it just shows the matter density when a given region is fully ionized, while it shows nothing (i.e., white) when a given region is fully neutral. The density fields are color-coded such that overdense regions are red and underdense regions are blue. We create this figure by interpolating between adjacent snapshots at a given lookback time. The length scale is linear in the co-moving units. The x-axis shows redshifts, while the y-axis shows h^{-1} Mpc.
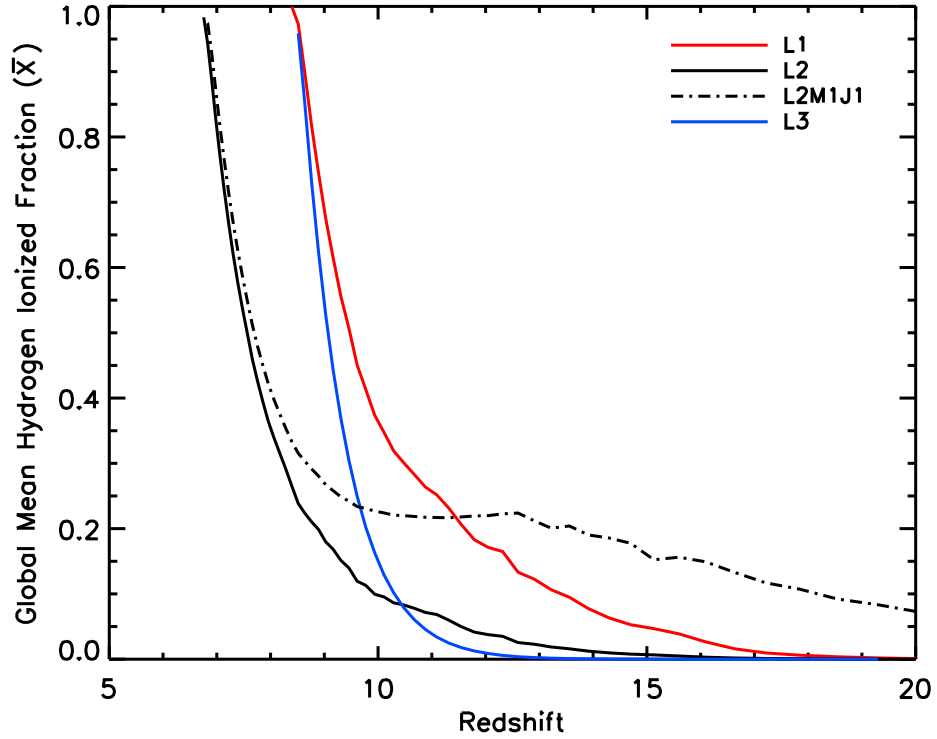
Figure 3.2: The global mean ionization history of our models (see Table 2.1 for the parameters of models). The mass-averaged hydrogen ionization fraction, $\bar{X}$, is plotted against z. Note how self-regulation results in an extended period of low-level ionization by comparing the case without self-regulation (L3 = HMACHs only) and that with self-regulation (L1 = HMACHs + LMACHs) [13]. A further extension occurs when MH sources are included, as well (i.e. compare L2 = HMACHs + LMACHs and L2M1J1 = L2 + MHs) [1].

reionization. These sources are defined as the halos with $M > 2.2 \times 10^9 M_\odot$ for L3; and with $M > 10^9$ $M_\odot$ (corresponding to $T_{\mathrm{vir}} \gtrsim 8 \times 10^4$ K at $z = 9$ from the TIS model of [15]) for the other configurations. These sources are believed to form stars even when immersed in ionized regions, due to the fact that their gravitational potential wells are deep enough to overcome Jeans-mass filtering.

3.2.2   HMACHs+LMACHs models

What about smaller-mass halos? LMACHs are more abundant; however, if they form inside the regions that have already been ionized, they would not act as sources of ionizing photons. This is because ionization heats the gas and makes its pressure too high for the gas to collapse into such small halos [12, and references therein].

When we include LMACHs and account for this "self-regulation" of reionization, we give LMACHs a higher efficiency, g_γ, than for HMACHs, as presumably it is easier for ionizing photons to escape from LMACHs than from HMACHs, and Pop III stars with a top-heavy initial mass function (IMF), which are capable of producing more ionizing photons than Pop II stars with a Salpeter IMF, are more likely to form in LMACHs. If HMACHs are formed by mergers of smaller-mass halos, for example, they are more likely to have enough metallicity to make the transition from Pop III to Pop II star formation and, hence, to a less efficient IMF.

There are two cases which have both HMACHs and LMACHs, and we shall call them L1 and L2. For L1, the efficiency parameter, g_γ, is chosen such

22

that the overlap redshift, $z_{ov} = 8.3$, is similar to that of L3, $z_{ov} = 8.4$ (see Table 2.1). For L2, g_γ is chosen such that z_{ov} is between 6 and 7, as suggested by the quasar absorption line observations.

For L2, we have another run with a much larger volume ($425\ h^{-1}$ Mpc) with 504^3 of radiative-transfer grids. Although it does not resolve LMACHs, we include LMACHs as a sub-grid model using correlation between average density of radiative transfer cells and number density of LMACHs similarly to how [1] included MHs in the simulation (Iliev et al. and Ahn et al. in preparation). This run gives $l_{limit} \sim 12000$. We shall call this configuration "XL2", as the volume for this run is bigger (hence the name, XL) than those runs with "L." This run will be used to check our method to correct for the missing velocity power.

3.2.3 HMACHs+LMACHs+MHs model

What about *even* smaller-mass sources? Gas in halos of masses between $10^5\ M_\odot$ and $10^8\ M_\odot$ is thought to cool via rotational and vibrational transitions of hydrogen molecules and form stars, until hydrogen molecules are dissociated by Lyman-Werner photons in the UV background from other sources [see [1] and references therein].

The MHs form earlier than LMACHs or HMACHs, and thus can start reionization of the universe earlier. However, as the star formation in MHs is vulnerable to Lyman-Werner photons, it gets suppressed wherever the intensity of the LW background rises above the threshold for suppression, locally at first,

23

and eventually globally. This adds another kind of "self-regulation" to the reionization history, with an even more extended phase of low-level ionization before MHs are eventually suppressed completely [1].

The effects of MHs have been added to L2 by [1], and we take one of the cases simulated there, L2M1J1, as our fiducial case with MHs. See Table 2.1 for the efficiency of MHs. "M" denotes the mass spectrum of Pop III stars in MHs, and "J" the threshold intensity of the Lyman-Werner photon background, above which the star formation in MHs is suppressed. In L2M1J1, each halo is assumed to host one Pop III star with mass of 300 $M_\odot$, and the assumed LW threshold is $J_{\mathrm{LW,th}} = 10^{-22}$ ergs^{-1}cm^{-2}sr^{-1}.

This parameter choice for M_* and $J_{\mathrm{LW,th}}$ is only illustrative. As we discussed in [1], the nature of the self-regulated suppression of MH star-formation is such that the contribution of MH stars to reionization rises to the point at which the global mean LW intensity reaches the threshold value for suppression. As long as MH stars dominate reionization (i.e. early phase), they continue to form at the global rate necessary to keep J_{LW} at this level, regardless of the value of M_*. For $M_* \gtrsim 100$ $M_\odot$, the ratio of ionizing to dissociating photons emitted per MH star is fixed, so their early contribution to reionization is also fixed by this self-regulation effect. Eventually, the LMACH and HMACH populations grow to dominate the LW background and suppress star formation inside MHs completely, thereafter. The value adopted for $J_{\mathrm{LW,th}}$ only affects the transition redshift at which this occurs somewhat (i.e. higher values allow MHs to contribute longer). In short, the reionization history is

relatively insensitive to the value adopted for M_*, if $M_* \gtrsim 100~M_\odot$, but some-what more sensitive to $J_{\rm LW,th}$. Recent suggestion that MH stars may form with lower values of M_* (e.g. $40~M_\odot$), perhaps with more than one star at a time, may alter some of these details, but the qualitative effect of self-regulation should remain. Similarly, the effect of a relative drift velocity between dark matter and baryons identified by [31], which tends to raise the minimum mass of MHs which typically form stars, is offset by a small shift in the timing of the early phase of MH-dominated reionization, as the exponential rise of MH abundances compensates at lower redshift.

Chapter 4

Results

Before presenting and discussing our predictions for the kSZ power spectrum, let us briefly comment on the global ionization history of the universe, which is the key to understanding the difference between our results and the previous ones. For more detailed discussion on the effects of self-regulation, see [12, 13] and [1].

Figure 3.1 shows how the reionization proceeds in our simulation boxes, while Figure 3.2 shows the mass-averaged ionization fraction of the universe as a function of redshift. Both figures show that inclusion of low-mass halos (LMACHs and MHs), which are self-regulated, significantly extends the ionization history of the universe toward higher redshift. Let us compare L1 and L3. As LMACHs form earlier, the universe begins to be ionized earlier in L1 than in L3. However, the universe does not get reionized quickly but keeps a low level of ionization for an extended period due to self-regulation of sources. Only after HMACHs start to dominate, at $z \sim 10$, does reionization proceed rapidly and finishes soon thereafter. In L3, with no LMACHs, by contrast, reionization proceeds rapidly from beginning to end because the abundance of HMACHs, the only sources, grows exponentially without any suppression

effects to self-regulate them. When MHs are included (L2M1J2), the universe begins to be ionized even earlier than the cases with HMACHs and LMACHs, and keeps a low-level ionization for a longer period.

These physically motivated yet somewhat complex reionization histories were not considered in any of the previous calculations of the kSZ power spectrum. In this section, we show that it is these new features in the reionization history that invalidate simple two-parameter descriptions of the amplitude of the kSZ power spectrum proposed by the previous study [2, 21, 35].

4.1 Impact of Inhomogeneous Reionization

First, it is useful to understand how important it is to include inhomogeneity (or patchiness) of reionization when computing the kSZ power spectrum. In order to see this, we create a homogeneous version of L3 ("L3-homogeneous"), in which we wipe out inhomogeneity of reionization by replacing the ionization fraction, χ, with its global average, $\bar{\chi}$ (see Figure 3.2). This then gives the transverse momentum power spectrum as $P_{q_\perp} = \bar{\chi}^2 P_{q_\perp}^{\mathrm{OV}}$, where $P_{q_\perp}^{\mathrm{OV}}$ is the OV spectrum given by Equation (2.5). We remind reader that, on the scales of interest to us in this power spectrum ($k \lesssim 1\ h\ \mathrm{Mpc}^{-1}$), the degree of non-linearity of the underlying density and velocity fields of the IGM is small enough that we can well approximate the kSZ power spectrum for this "homogeneous" ionization case by the assumption of linear perturbations inherent in Equation (2.5) (see Section 2.2 and the left panel of Figure 2.1). We use this momentum power spectrum in Equation (2.3) to obtain the kSZ

27

power spectrum for "L3-homogeneous." Thus, "L3" and "L3-homogeneous" have exactly the same average reionization history, while spatial fluctuations of ionization fraction are included only in L3. We find that L3 yields an order-of-magnitude larger power spectrum than L3-homogeneous that is consistent with findings in [14](see Figure 4.1).

In order to see the effect of inhomogeneous reionization on the kSZ power spectrum in more detail, we show the contribution from a given comoving distance to the kSZ power spectrum at $l = 3000$, $dC_{l=3000}^{\rm kSZ}/ds$, in Figure 4.2. While both L3 and L3-homogeneous converge to the same $dC_{l=3000}^{\rm kSZ}/ds$ after the universe becomes fully ionized, we find a clear enhancement of the power when the ionization fraction is less than unity, $z > z_{\rm ov} = 8.4$. The maximum contribution occurs when the universe is half ionized. One can see this visually in the middle (L3) and bottom (L3-homogeneous) panels of Figure 4.2: L3 is clearly more patchy than L3-homogeneous.

The angular scale for $l = 3000$ roughly corresponds to the co-moving length of 15 h^{-1} Mpc during the reionization era ($z \sim 10$). The contribution to the kSZ power spectrum continues to grow until the typical comoving size of ionized bubbles reaches 15 h^{-1} Mpc. In our models, this occurs when the universe is half ionized. After this epoch bubbles grow bigger than 15 h^{-1} Mpc, and thus the ionization field is no longer patchy on the scale of 15 h^{-1} Mpc. This explains why the contribution to the kSZ power spectrum at $l = 3000$ decreases after the half-ionization epoch. (By the same token, a plot like that for the inhomogeneous case L3 in Figure 4.2 but for $l > 3000$ would

look similar but with the peak shifted to higher z, when ionized patches were smaller-scale.)

4.2   Impact of LMACHs

How does the presence of LMACHs and self-regulation affect the kSZ power spectrum? To answer this we compare L1 and L3, which are mostly similar except that L1 has low-mass halos (10^8 $M_\odot$ $<$ M $<$ 2.2×10^9 $M_\odot$) with most of them being LMACHs. While they finish reionization at nearly the same redshift, L1 begins ionization earlier due to LMACHs and gives an extended period of low ionization due to self-regulation (see Figure 3.2).

Figure 4.1 shows that L1 and L3 give similar kSZ power spectra at $l \lesssim 3000$, while at higher multipoles L1 becomes significantly greater than L3. This is because there are numerous ionized bubbles created by LMACHs at high redshifts, which give significant contributions to the small-scale kSZ power spectrum. Although it would be a challenge for current surveys, future measurements of D_l^{kSZ} with 10% accuracy over a wide range of multipoles can distinguish between the predictions of L1 and L3, shedding light on the roles of LMACHs during the reionization.

We compare the contributions from a given comoving distance to the kSZ power spectrum at $l = 3000$, $dC_{l=3000}^{\mathrm{kSZ}}/ds$, for L1 and L3 in Figure 4.3. As expected, L1 has larger contributions at higher redshifts ($z \gtrsim 10$) due to LMACHs. On the other hand, L3 has larger contributions at lower redshifts ($z \lesssim 10$), as it is more patchy due to the absence of smaller bubbles around

LMACHs (see the middle (L3) and bottom (L1) panels of Figure 4.3). In L1, bubbles around LMACHs do not grow much because of self-regulation.

In the left panel of Figure 4.4, we show the cumulative contributions to the kSZ power spectrum at $l = 3000$ below a given maximum redshift, z. This also shows that L1 receives larger contributions from higher redshifts than L3: 20% of the total power in L1 comes from $z > 11$, while only a few percent of the total power in L3 comes from $z > 11$. Similarly, the right panel of Figure 4.4 shows that 20% of the total power in L1 comes from when the ionization fraction is less than 0.25, which is consistent with the ionization history above $z = 11$ shown in Figure 3.2. This extended tail has important implications for the interpretation of the kSZ power spectrum, as we shall discuss in Section 5.

4.3 Impact of Minihalos

What about MHs? We compare L2 and L2M1J1, which have the same efficiency parameters for HMACHs and LMACHs, but only L2M1J1 considering MHs. While L2 and L2M1J1 finish reionization at almost the same redshift, L2M1J1 begins ionization much earlier due to MHs and gives a significantly more extended period of low ionization due to self-regulation (see Figure 3.2).

Figure 4.1 shows that L2 and L2M1J1 give similar kSZ power spectra at $l \lesssim 5000$, while at higher multipoles L2M1J1 becomes greater than L2. The reason is the same as that for L1 versus L3: there are numerous ionized

bubbles created by MHs at high redshifts, which contribute to the small-scale kSZ power spectrum.

While L2M1J1 begins reionization much earlier and thus has more contribution from high redshifts to the kSZ power spectrum, the actual magnitude of the high-redshift contribution is modest. This is because of self-regulation: self-regulation prevents bubbles around MHs from growing, and thus we end up having numerous small bubbles filling space nearly uniformly. This results in a lesser degree of patchiness, hence a modest contribution to the kSZ power spectrum at $l = 3000$. One can see this visually in the middle (L2M1J1) and bottom (L2) panels of Figure 4.5. As a result, the situation is similar to that for L1 versus L3: 20% of the total power at $l = 3000$ in L2M1J1 comes from $z > 10$, while only 5% of the total power in L2 comes from $z > 10$.

It is interesting that all the models with self-regulation (L1, L2, and L2M1J1) lie on top of each other when the cumulative contribution is shown as a function of the mean ionization fraction (see the right panel of Figure 4.4), whereas the model that does not have self-regulation (L3) is a clear outlier. Whether this is merely a coincidence or a unique feature of self-regulation is unclear due to the limited number of samples.
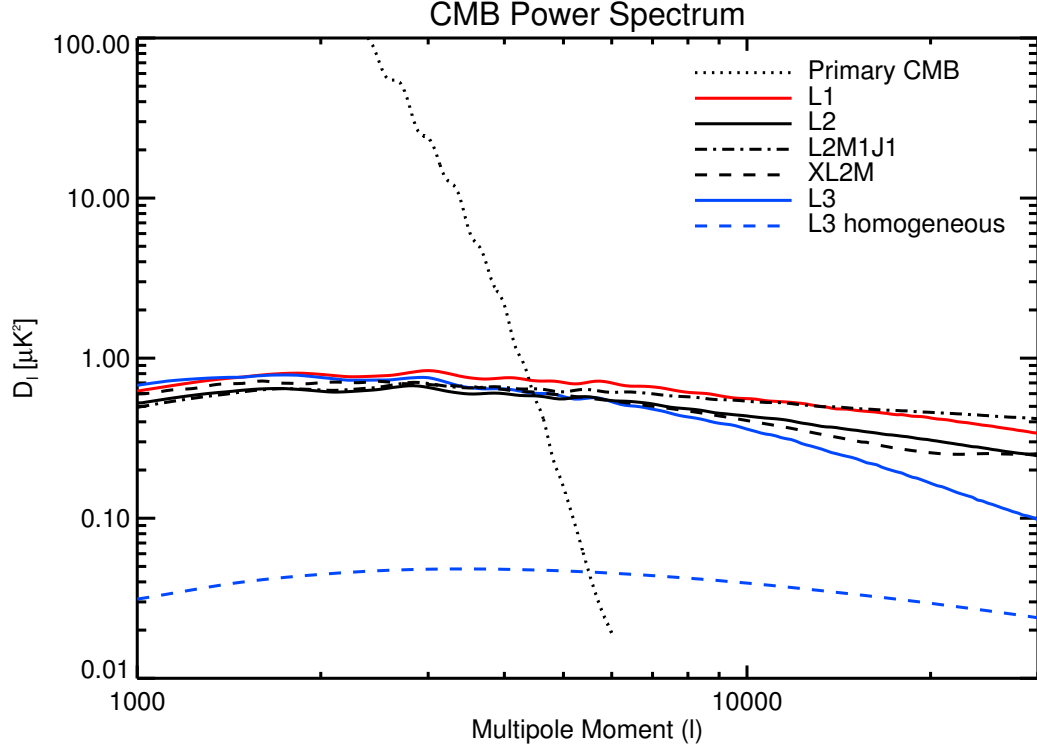
Figure 4.1: Predicted kSZ power spectra, D_l^{kSZ}, from $z > z_{\mathrm{ov}}$ for the models discussed in this work (see Table 2.1 for the parameters of models). $z_{\mathrm{ov}} =$ 8.3, 6.8, 6.8, 6.8 and 8.4 for L1, L2, XL2, L2M1J1 and L3, respectively. The box size of L1, L2, L2M1J1 and L3 is 114 h^{-1} Mpc, while that of XL2 is 425 h^{-1} Mpc. The model parameters of XL2 are the same as those of L2, and thus XL2 provides a useful check of the way we correct for the missing velocity power in 114 h^{-1} Mpc-box simulations (see Appendix B for details). The primary CMB power spectrum is also shown.
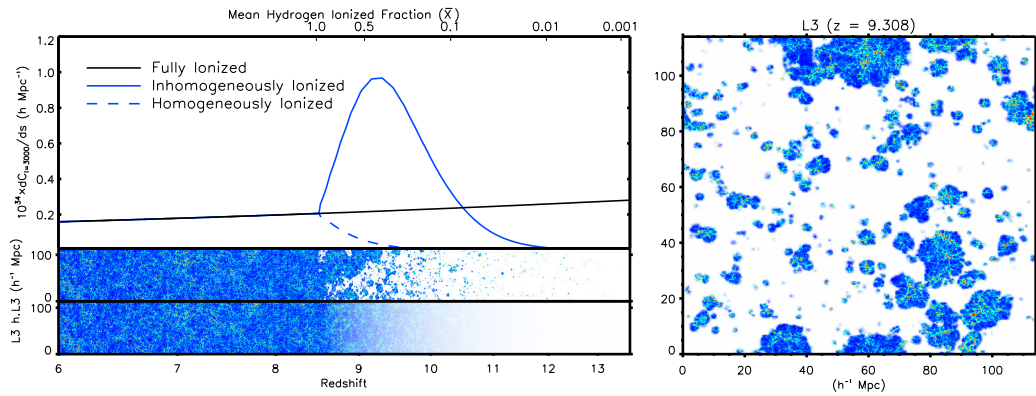
Figure 4.2: Left: The top panel shows the contribution from a given comoving distance to the kSZ power spectrum at $l = 3000$, $dC_{l=3000}^{\text{kSZ}}/ds$. The solid line with a peak shows L3, the dashed line shows L3-homogeneous, and the nearly-horizontal solid line shows the fully-ionized case. The middle panel is the same as the bottom panel of Figure 3.1. The bottom panel shows L3-homogeneous, i.e., the density distribution multiplied by the average ionization fraction. Right: A snapshot of L3 at $z = 9.3$, which gives the maximum contribution to the kSZ power spectrum at $l = 3000$.

33
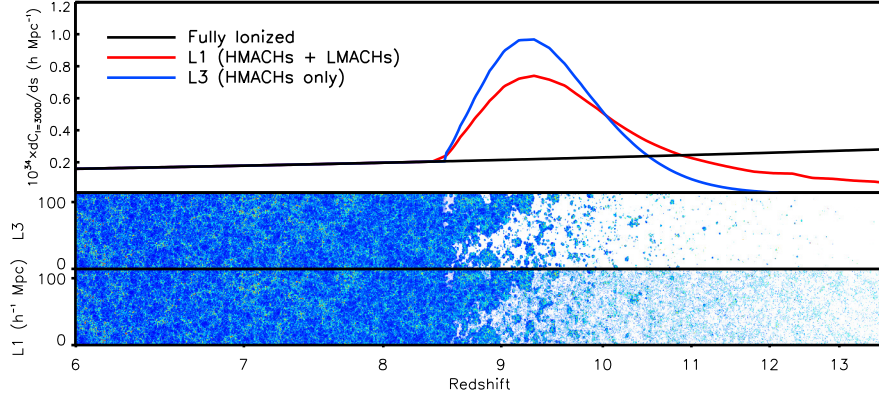
Figure 4.3: Same as the left panel of Figure 4.2, but for comparing L1 (bottom panel) and L3 (middle panel). See Table 2.1 for the parameters of L1 and L3.
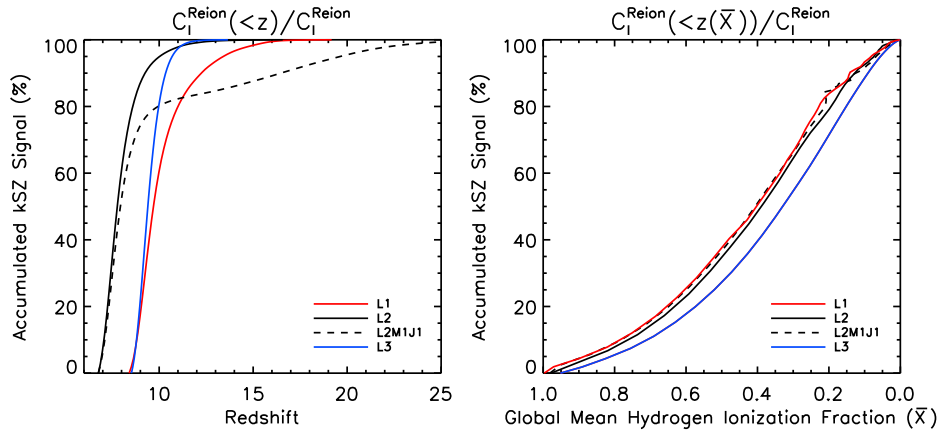
Figure 4.4: Cumulative reionization kSZ power spectrum at $l = 3000$ as a function of the maximum redshift (Left) and the mean ionization fraction (Right).

34
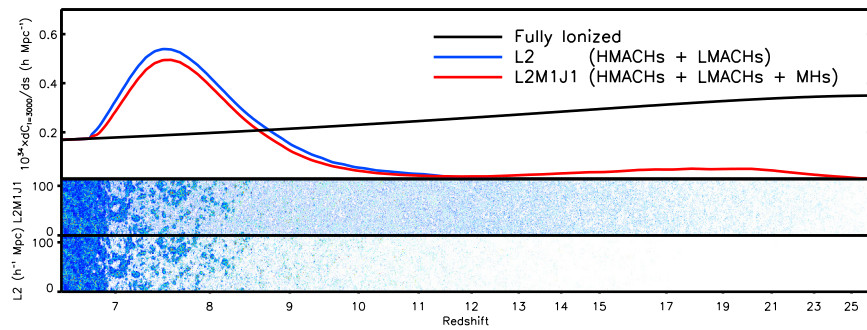
Figure 4.5: Same as the left panel of Figure 4.2, but for comparing L2 (bottom panel) and L2M1J1 (middle panel). See Table 2.1 for the parameters of L2 and L2M1J1.

Chapter 5

Spot checking the previous constraints on the duration of reionization: more extended histories can give similar kSZ signals

What determines the amplitude of the kSZ power spectrum? Recent studies using semi-numerical reionization models [2, 21, 35] claim that the amplitude of the kSZ power spectrum at $l = 3000$ can be described by a two-parameter family: the redshift of half-ionization, $z_{50\%}$, and the duration of reionization defined as $\Delta z \equiv z_{99\%} - z_{20\%}$ [35] or $\Delta z \equiv z_{75\%} - z_{25\%}$ [2, 21]. None of these studies included the effects of self-regulated reionization, and thus the reionization histories explored in these studies are roughly symmetric about the epoch of half-ionization.

Figure 2 of [35] shows that the kSZ power spectrum at $l = 3000$ increases by a factor of two as the duration of reionization increases from $\Delta z = 2$ to 4. Figure 10 of [21] shows that, for a half-ionization redshift of $z_{50\%} = 9$, the kSZ power spectrum at $l = 3000$ increases by a factor of 1.4 as the duration of reionization increases from $\Delta z = 1.3$ to 2.6. The former gives a scaling of $D_{l=3000}^{\mathrm{kSZ}} \propto (z_{99\%} - z_{20\%})$, whereas the latter gives $D_{l=3000}^{\mathrm{kSZ}} \propto (z_{75\%} - z_{25\%})^{0.5}$, for a fixed half-ionization redshift. More recently, using a new semi-numerical method based on a correlation between the smoothed density field and the

36

redshift-of-reionization field found from radiation-hydro simulations of [3], [2] calculate the kSZ power spectrum coming from $z > 5.5$ and obtain the following scaling relation:

$$D_{l=3000}^{\text{kSZ,z}>5.5} = 2.02 \ \mu\text{K}^2 \left[\left(\frac{1+\bar{z}}{11} \right) - 0.12 \right] \left(\frac{\Delta z}{1.05} \right)^{0.47}, \tag{5.1}$$

where $\Delta z = z_{75\%} - z_{25\%}$ and $\bar{z}$ is the mean value of the redshift-of-reionization field, which is approximately equal to the half-ionization redshift, $z_{50\%}$.

Table 5.1: Global reionization history and kSZ signal

Label	$z_{50\%}$	$z_{99\%} - z_{20\%}$	$z_{75\%} - z_{25\%}$	z_{ov}	$D_{l=3000}^{\text{kSZ,z}>5.5}$	$D_{l=3000}^{\text{kSZ,z}<z_{\text{ov}} 1}$	$D_{l=3000}^{\text{kSZ,z}>z_{\text{ov}}}$	$D_{l=3000}^{\text{kSZ,total}}$
L1	9.5	3.2	2.2	8.3	1.27	1.94	0.83	2.77
L2	7.6	2.1	1.4	6.8	0.87	1.69	0.66	2.35
L2M1J1	7.7	6.5	2.1	6.8	0.90	1.69	0.69	2.38
L3	9.1	1.3	0.9	8.4	1.20	1.96	0.75	2.71

Our predictions for $D_{l=3000}^{\text{kSZ}}$ are summarized in Table 5.1. Among the models we have explored in this paper, L3 (which contains only HMACHs and does not have self-regulation) closely matches the scenarios explored in the above studies. Using $z_{50\%} = 9.1$ and $z_{75\%} - z_{25\%} = 0.9$ we find for L3, Equation (5.1) gives $D_{l=3000}^{\text{kSZ,z}>5.5} = 1.5 \ \mu\text{K}^2$. This is in a reasonable agreement with our result,[2] $D_{l=3000}^{\text{kSZ,z}>5.5} = 1.2 \ \mu\text{K}^2$.

However, the above formula significantly overestimates the amplitude of the kSZ power spectrum for L1: Equation (5.1) gives $D_{l=3000}^{\text{kSZ,z}>5.5} = 2.4 \ \mu\text{K}^2$,

---

[2]In order to compute $D_{l=3000}^{\text{kSZ,z}>5.5}$, we calculate the contribution from z between 5.5 and z_{ov} using the fully-ionized formula, $P_{q_\perp} = P_{q_\perp}^{\text{OV}}$, and add it to $D_{l=3000}^{\text{kSZ,z}>z_{\text{ov}}}$ shown in the seventh column of Table 5.1.

whereas we find $D_{l=3000}^{\text{kSZ,z}>5.5} = 1.3 \; \mu\text{K}^2$. In other words, despite the fact that L1 has a significantly more extended duration of reionization than L3 (by a factor of more than two), $z_{75\%} - z_{25\%} = 2.2$, the amplitude of the kSZ power spectrum increases only by 8%. Similarly, Equation (5.1) gives $D_{l=3000}^{\text{kSZ,z}>5.5} = 1.5$ and 1.9 μK^2 for L2 and L2M1J1, respectively, whereas we find 0.9 μK^2 for both cases. Therefore, we conclude that Equation (5.1) is valid only for simple scenarios where the reionization history is roughly symmetric about the half-ionization redshift, but is invalid when self-regulation is included. Similar conclusions apply to [35] and [21].

Our results show that self-regulation makes the duration of reionization significantly more extended without changing the amplitude of the kSZ power spectrum very much. In other words, an extended period of low-level ionization in $z > z_{50\%}$ does not make much contribution to the kSZ power spectrum at $l = 3000$.

Chapter 6

Conclusion

In this paper, using the state-of-the-art reionization simulations incorporating the effects of self-regulated reionization [1, 13], we have computed the power spectrum of the kSZ effect from the EOR. Unlike the previous work which created maps and computed two-dimensional Fourier transforms from the maps, we have computed the kSZ power spectrum from a line-of-sight integral of the transverse momentum power spectrum of ionized gas. We present a method to statistically correct for the missing velocity power in Appendix B, and verify the accuracy of our method by comparing the results from large- (425 Mpc/h) and small-box (114 Mpc/h) simulations.

We find that the kSZ power spectrum is a sensitive probe of patchiness of reionization: patchiness increases the amplitude of the kSZ power spectrum by an order of magnitude. The maximum contribution occurs when the angular sizes of ionized bubbles are close to those corresponding to a given multipole.

While inclusion of small-mass halos such as LMACHs and MHs makes the beginning of reionization earlier, self-regulation significantly slows down the progress of reionization [1, 12, 13]. This results in an extended period of

39

low-level ionization before more massive HMACHs dominate and finish reion-
ization. We find that such an extended period of low-level ionization does
not, however, make much of a contribution to the kSZ power spectrum at
$l = 3000$: $D_{l=3000}^{\mathrm{kSZ}}$ changes only by $\sim 10\%$ despite the fact that the duration of
reionization increases by a factor of more than two.

Our results qualitatively change the conclusions reached by the previ-
ous work which did not include self-regulation. Recent work [2, 21, 35] assumes
that $D_{l=3000}^{\mathrm{kSZ}}$ can be adequately parameterized by the redshift of half-ionization,
$z_{50\%}$, and the duration of reionization, Δz. While our result for the simplest
model of reionization without self-regulation (L3) agrees with the scaling for-
mula of [2] (Equation 5.1), our results for the models with self-regulation do
not agree with it: specifically, the amplitude of the kSZ effect is no longer corre-
lated well with the duration of the reionization. This is because self-regulation
gives an extended period of low-level reionization only for $z > z_{20\%}$, while the
simple models adopted by these other treatments have a roughly symmetric
reionization history about $z = z_{50\%}$, for which a longer duration thus implies
a longer period of patchy state with a significant ionization across $z = z_{50\%}$.
Therefore, a more accurate scaling formula is required to take into account the
asymmetric reionization history typical of self-regulated reionization.

Going beyond $l = 3000$, we find that LMACHs and MHs do have a
considerable impact on the kSZ power spectrum on smaller angular scales.
For example, $D_{l=10000}^{\mathrm{kSZ}}$ is boosted by 60% and 25% when LMACHs and MHs
are included, respectively. Even though measurements of the kSZ power spec-

trum at $l > 3000$ would be a challenge for the moment due to contamination by extragalactic point sources and tSZ, future multi-wavelength observations may allow us to determine the kSZ power spectrum from the EOR over a wide range of multipoles. Such measurements will provide us with valuable additional information on the nature of the ionizing sources and the history of reionization.

How do our calculations compare with these current observational constraints? In order to obtain the total kSZ signal from both reionization and post-reionization contributions, we take the "CSF" (cooling and star formation) post-reionization model of [29] that approximately incorporates the Jeans-filtering of $P_{q_\perp}$ due to shock heating in halos and in the IGM. The post-reionization kSZ signal computed from their scaling relation and the total kSZ signal (i.e., the sum our reionization calculation and their post-reionization calculation) are shown in the sixth and seventh columns of Table 5.1, respectively. We find that all of our predictions are consistent with the 95% CL upper bound on the total signal from SPT, $D_{l=3000}^{\text{kSZ,total}} < 2.8 \ \mu K^2$ [24]. Therefore, we conclude that the current data are consistent with our understanding of the physics of reionization.

Appendices

Appendix A

Derivation of the power spectrum of the kSZ effect

A.1 Suppression of longitudinal modes

An important observation of the nature of kSZ is that it is given by the *transverse* (vector-mode or spin-1) momentum field, and the longitudinal contribution is suppressed. To show this, we Fourier transform Equation (2.2):

$$\frac{\Delta T}{T}(\hat{\gamma}) = -\frac{\sigma_T n_{e,0}}{c} \int \frac{ds}{a(s)^2} e^{-\tau} \int \frac{d^3k}{(2\pi)^3} [\hat{\gamma} \cdot \tilde{\mathbf{q}}(\mathbf{k}, s)] e^{-i\mathbf{k}\cdot(s\hat{\gamma})}. \qquad (A.1)$$

Decomposing the momentum vector in Fourier space, $\tilde{\mathbf{q}}$, into the longitudinal component, $\tilde{q}_{\parallel} \equiv \tilde{\mathbf{q}} \cdot \hat{k}$, and the transverse component, $\tilde{q}_{\perp} \equiv |\tilde{\mathbf{q}} - \hat{k}(\tilde{\mathbf{q}} \cdot \hat{k})|$, we obtain

$$\frac{\Delta T}{T}(\hat{\gamma}) = -\frac{\sigma_T n_{e,0}}{c} \int \frac{ds}{a(s)^2} e^{-\tau} \int \frac{d^3k}{(2\pi)^3}$$

$$\left[x\tilde{q}_{\parallel}(\mathbf{k}, s) + \cos(\phi_{\hat{q}} - \phi_{\hat{\gamma}})(1 - x^2)^{1/2}\tilde{q}_{\perp}(\mathbf{k}, s) \right] e^{-iksx}, \quad (A.2)$$

where $x \equiv \hat{k} \cdot \hat{\gamma}$, and $\phi_{\hat{q}}$ and $\phi_{\hat{\gamma}}$ are the angles that $\mathbf{k}$ makes with $\tilde{\mathbf{q}}$ and $\hat{\gamma}$, respectively.

If the factor e^{iksx} oscillates much more rapidly than the other quantities, the integral over s will be small due to cancellation. Recalling that $a(s)$, $\tau(s)$,

and $\tilde{\mathbf{q}}$ all vary over the Hubble length scale, kx should be much smaller than H/c in order to avoid the cancellation. Namely, either the wavelength should be longer than the Hubble length, i.e., $k \lesssim H/c$, or the mode should be nearly perpendicular to the line-of-sight direction, i.e., $x \approx 0$. The former does not contribute much because the amplitude of such a long-wavelength mode is small. Thus, only the modes that are perpendicular to the line-of-sight direction, $x \approx 0$, have a chance to contribute to the kSZ signal.

However, in this configuration, the longitudinal component of the momentum field is also perpendicular to the line-of-sight, and vanishes when taken a dot-product with the line-of-sight, i.e., $x\tilde{q}_{\parallel} \approx 0$. Therefore, only the transverse mode survives in the integral, giving

$$\frac{\Delta T}{T}(\hat{\gamma}) = -\frac{\sigma_T n_{e,0}}{c} \int \frac{ds}{a(s)^2} e^{-\tau} \int \frac{d^3k}{(2\pi)^3} \cos(\phi_{\hat{q}} - \phi_{\hat{\gamma}})(1 - x^2)^{1/2} \tilde{q}_{\perp}(\mathbf{k}, s) e^{-iksx}.$$
(A.3)

A.2   Angular Power Spectrum

Here, we follow steps similar to those in Chapter 7.3 of [33] to derive the angular power spectrum of CMB fluctuations induced by the kSZ effect.

Spherical harmonic decomposition of Equation (A.3) gives

$$
a_{lm} = \int d^2\hat{\gamma}\, Y_l^{m*}(\hat{\gamma})\frac{\Delta T}{T}(\hat{\gamma})
$$

$$
= -\frac{\sigma_T n_{e,0}}{c}\int d^2\hat{\gamma}\, Y_l^{m*}(\hat{\gamma})\int\frac{ds}{a(s)^2}e^{-\tau}\int\frac{d^3k}{(2\pi)^3}\cos(\phi_{\hat{q}}-\phi_{\hat{\gamma}})(1-x^2)^{1/2}\tilde{q}_\perp(\mathbf{k},s)e^{-iksx}
$$

$$
\equiv -\frac{\sigma_T n_{e,0}}{c}\int\frac{d^3k}{(2\pi)^3}\, f_{lm}(\mathbf{k}), \tag{A.4}
$$

where

$$
f_{lm}(\mathbf{k}) \equiv \int d^2\hat{\gamma}\, Y_l^{m*}(\hat{\gamma})\int\frac{ds}{a(s)^2}e^{-\tau}\cos(\phi_{\hat{q}}-\phi_{\hat{\gamma}})(1-x^2)^{1/2}\tilde{q}_\perp(\mathbf{k},s)e^{-iksx}
$$

$$
= \int d^2\hat{\gamma}\, Y_l^{m*}(\hat{\gamma})\int\frac{ds}{a(s)^2}e^{-\tau}\cos(\phi_{\hat{q}}-\phi_{\hat{\gamma}})(1-x^2)^{1/2}\tilde{q}_\perp(\mathbf{k},s)
$$

$$
\times 4\pi\sum_{LM}(-i)^L j_L(ks)Y_L^M(\hat{\gamma})Y_L^{M*}(\hat{k}). \tag{A.5}
$$

We first choose a convenient coordinate system in which the z-direction lies on that of the mode vector, i.e., $\hat{k}=\hat{z}$, and the azimuthal direction is the same as the direction of the momentum vector, i.e., $\phi_{\hat{q}}=0$. In this case,

$Y_L^{M*}(\hat{k})$ simplifies to $Y_L^{M*}(\hat{z}) = \delta_{M0}\sqrt{\frac{2L+1}{4\pi}}$, giving

$$f_{lm}(k\hat{z}) = \sqrt{4\pi} \int \frac{ds}{a(s)^2} e^{-\tau} \tilde{q}_\perp(\mathbf{k}, s) \sum_L (-i)^L \sqrt{2L+1} j_L(ks)$$

$$\int d^2\hat{\gamma}\, Y_L^0(\hat{\gamma})\, \cos\phi\, \sin\theta\, Y_l^{m*}(\hat{\gamma})$$

$$= \sqrt{\frac{8\pi^2}{3}} \int \frac{ds}{a(s)^2} e^{-\tau} \tilde{q}_\perp(\mathbf{k}, s) \sum_L (-i)^L \sqrt{2L+1} j_L(ks)$$

$$\int d^2\hat{\gamma}\, Y_L^0(\hat{\gamma})\, \left[Y_1^{-1}(\hat{\gamma}) - Y_1^1(\hat{\gamma}) \right] Y_l^{m*}(\hat{\gamma}), \tag{A.6}$$

where θ and $\phi = \phi_{\hat{\gamma}}$ determine the line-of-sight vector as $\hat{\gamma} = (\cos\theta\sin\phi, \sin\theta\sin\phi, \cos\phi)$.

The integral over $\hat{\gamma}$ can be computed using,

$$\int d^2\hat{\gamma}\, Y_L^M(\hat{\gamma})\, Y_\Lambda^\mu(\hat{\gamma})\, Y_l^{m*}(\hat{\gamma}) = \sqrt{\frac{(2\Lambda+1)(2l+1)}{4\pi(2L+1)}}$$

$$\times C_{l\Lambda}(L, M; m, -\mu) C_{l\Lambda}(L, 0; 0, 0) \delta_{M, m-\mu}, \tag{A.7}$$

where $C_{l\Lambda}(L, M; m, \mu)$ is the Clebsch-Gordan coefficient for adding the angular momentum quantum numbers (l, m) and (Λ, μ) and for forming (L, M). In our case, we have

$$f_{l,m=\pm 1}(k\hat{z}) = \sqrt{2\pi(2l+1)} \int \frac{ds}{a(s)^2} e^{-\tau} \tilde{q}_\perp(\mathbf{k}, s) \sum_L (-i)^L j_L(ks) \times$$

$$\left[\pm C_{l1}(L, 0; \pm 1, \mp 1) C_{l1}(L, 0; 0, 0)) \right]. \tag{A.8}$$

Thus, the relevant coefficients are

$$C_{l1}(l+1,0;0,0) = \sqrt{\frac{l+1}{2l+1}},$$

$$C_{l1}(l+1,0;\pm 1,\mp 1) = \sqrt{\frac{l}{2(2l+1)}},$$

$$C_{l1}(l,0;0,0) = 0,$$

$$C_{l1}(l-1,0;0,0) = \sqrt{\frac{l}{2l+1}},$$

$$C_{l1}(l-1,0;\pm 1,\mp 1) = \sqrt{\frac{l+1}{2(2l+1)}}. \tag{A.9}$$

Putting these together gives

$$
\begin{aligned}
f_{l,m=\pm 1}(k\hat{z}) &= (-i)^{l+1}\sqrt{\frac{\pi l(l+1)}{2l+1}} \int \frac{ds}{a(s)^2} e^{-\tau} \tilde{q}_{\perp}(\mathbf{k},s) \left[j_{l+1}(ks) + j_{l-1}(ks) \right] \\
&= (-i)^{l+1}\sqrt{\pi l(l+1)(2l+1)} \int \frac{ds}{a(s)^2} e^{-\tau} \tilde{q}_{\perp}(\mathbf{k},s) \frac{j_l(ks)}{ks}. \tag{A.10}
\end{aligned}
$$

Now, we get back to the observer's frame by applying the standard rotation operator, $S(\hat{q})$, that takes the z-direction into $\hat{k}$. This gives

$$f_{lm}(\mathbf{k}) = \sum_{m'=\pm 1} D^l_{m,m'}(S(\hat{k})) f_{lm'}(k\hat{z}), \tag{A.11}$$

where $D^l_{mm'} = \langle l,m'|S|l,m \rangle$ is the matrix representation of the finite rotation

of an initial state (l, m) into a final state (l, m'). We obtain

$$
a_{lm} = -\frac{\sigma_T n_{e,0}}{c} \int \frac{d^3 k}{(2\pi)^3} \sum_{m'=\pm 1} D^l_{m,m'}(S(\hat{k}))
$$

$$
(-i)^{l+1} \sqrt{\pi l(l+1)(2l+1)} \int \frac{ds}{a(s)^2} e^{-\tau} \tilde{q}_\perp(\mathbf{k}, s) \frac{j_l(ks)}{ks}. \quad \text{(A.12)}
$$

Finally, we calculate the angular power spectrum from $\langle a_{lm} a^*_{l'm'} \rangle = C_l \delta_{ll'} \delta_{mm'}$ and obtain

$$
C_l = \frac{l(l+1)}{\pi} \left(\frac{\sigma_T n_{e,0}}{c} \right)^2 \int \frac{ds}{a(s)^2} e^{-\tau(s)} \int \frac{ds'}{a(s')^2} e^{-\tau(s')} \int k^2 dk \frac{j_l(ks)}{ks} \frac{j_l(ks')}{ks'} P_{q_\perp}(k, s),
$$
$$
\text{(A.13)}
$$

where $P_{q_\perp}$ is the power spectrum of $\tilde{\mathbf{q}}_\perp$ defined by $(2\pi)^3 P_{q_\perp}(k) \delta^D(\mathbf{k} - \mathbf{k}') = \langle \tilde{\mathbf{q}}_\perp(\mathbf{k}) \tilde{\mathbf{q}}^*_\perp(\mathbf{k}') \rangle$. Here, we have used the identity,

$$
\int d^2 \hat{k} \; D^l_{m,\pm 1}(S(\hat{k})) D^{l'*}_{m',\pm 1}(S(\hat{k})) = \frac{4\pi}{2l+1} \delta_{mm'} \delta_{ll'}. \quad \text{(A.14)}
$$

The integral over k can be performed with Limber's approximation: when a function $g(k, s)$ varies much more slowly than the spherical Bessel function, one can approximate the integral as

$$
\int k^2 dk \, j_l(ks) j_l(ks') g(k, s) \approx \frac{\pi}{2} \frac{\delta^D(s - s')}{s^2} g\left(k = \frac{l}{s}, s \right). \quad \text{(A.15)}
$$

With this approximation, we finally obtain the desired formula for the kSZ power spectrum:

$$
C_l = \left(\frac{\sigma_T n_{e,0}}{c} \right)^2 \int \frac{ds}{s^2 a(s)^4} e^{-2\tau(s)} \frac{P_{q_\perp}(k = l/s, s)}{2}. \quad \text{(A.16)}
$$

This is Equation (2.3).

Appendix B

Correcting for the Missing Power in Simulations

The transverse momentum power spectrum at a given wavenumber, $P_{q_\perp}(k)$, receives contributions from the density and velocity auto/cross power spectra at various wavenumbers via Equation (2.6). As a result, $P_{q_\perp}$ computed from a simulation with a finite box suffers from a loss of power due to the lack of modes whose wavelength is greater than the size of the box [14].

The missing power arises because we do not have $P_{\chi(1+\delta),\chi(1+\delta)}(k)$, $P_{vv}(k)$, or $P_{\chi(1+\delta),v}(k)$ for $k < k_{\text{box}} \equiv 2\pi/l_{\text{box}}$, where l_{box} is the size of the box. In Equation (2.6), this leads to the missing contributions in $|\mathbf{k}'| < k_{\text{box}}$ and $|\mathbf{k} - \mathbf{k}'| < k_{\text{box}}$. Estimating and correcting for the missing power thus requires the knowledge of the large-scale limit of $P_{\chi(1+\delta),\chi(1+\delta)}$, P_{vv}, and $P_{\chi(1+\delta),v}$.

For the homogeneous reionization case, it is straightforward to recover the missing power, as the large-scale limits of P_{vv}, $P_{\chi(1+\delta),\chi(1+\delta)}(= \bar{\chi}^2 P_{\delta\delta})$, and $P_{\chi(1+\delta),v}(= \bar{\chi} P_{\delta v})$ are precisely known by the cosmological linear perturbation theory. Using $P_{\delta\delta}$ from the linear theory and the linear relation, $P_{vv} = (\dot{a}f/k)^2 P_{\delta\delta}$, we find that the missing-power-corrected momentum power spectrum from the N-body simulation agrees precisely with the expected OV

spectrum (see Figure 2.1). Note that most of the missing power comes from $P_{\delta\delta}(|\mathbf{k} - \mathbf{k}'|)P_{vv}(k')$ in $k' < k_{\text{box}}$ because of the relation, $\mathbf{v}(\mathbf{k}) \propto \delta(\mathbf{k})/k$, in the large-scale limit.

For the inhomogeneous reionization case, we do not have a precise way to calculate the ionized density power, $P_{\chi(1+\delta),\chi(1+\delta)}$, in the large-scale limit; however, we expect that the density field and the ionization field are reasonably flat at the scales larger than the box size, and correct for the missing bulk velocity of the box. Therefore, we expect that the term $P_{\chi(1+\delta),\chi(1+\delta)}(|\mathbf{k} - \mathbf{k}'|)P_{vv}(k')$ in $k' < k_{\text{box}}$ captures most of the missing power, as we have seen from the homogeneous reionization case above. With this approximation, the missing power in the inhomogeneously ionized regime is given by

$$P_{q_\perp}^{\text{Missing}}(k, z) = \int_{k < k_{\text{box}}} \frac{d^3 k'}{(2\pi)^3} (1 - \mu'^2) P_{\chi(1+\delta),\chi(1+\delta)}(|\mathbf{k} - \mathbf{k}'|)P_{vv}(k'). \quad \text{(B.1)}$$

In order to check the accuracy of Equation (B.1), we compare the missing-power-corrected momentum power spectrum from the box of 114 h^{-1} Mpc (black solid line; denoted as L2) with that from a larger box of 425 h^{-1} Mpc (black dashed line; XL2) in Figure 4.1. We find a very good agreement between the two, confirming the robustness of our correction for the missing power.

Bibliography

[1] K. Ahn, I. T. Iliev, P. R. Shapiro, G. Mellema, J. Koda, and Y. Mao. Detecting the Rise and Fall of the First Stars by Their Impact on Cosmic Reionization. *ApJ*, 756:L16, September 2012.

[2] N. Battaglia, A. Natarajan, H. Trac, R. Cen, and A. Loeb. Reionization on Large Scales III: Predictions for Low-ell Cosmic Microwave Background Polarization and High-ell Kinetic Sunyaev-Zel'dovich Observables. *arXiv:1211.2832*, November 2012.

[3] N. Battaglia, H. Trac, R. Cen, and A. Loeb. Reionization on Large Scales I: A Parametric Model Constructed from Radiation-Hydrodynamic Simulations. *arXiv:1211.2821*, November 2012.

[4] T. M. Crawford, K. K. Schaffer, S. Bhattacharya, K. A. Aird, B. A. Benson, L. E. Bleem, J. E. Carlstrom, C. L. Chang, H. Cho, A. T. Crites, T. de Haan, M. A. Dobbs, J. Dudley, E. M. George, N. W. Halverson, G. P. Holder, W. L. Holzapfel, S. Hoover, Z. Hou, J. D. Hrubes, R. Keisler, L. Knox, A. T. Lee, E. M. Leitch, M. Lueker, D. Luong-Van, J. J. McMahon, J. Mehl, S. S. Meyer, M. Millea, L. M. Mocanu, J. J. Mohr, T. E. Montroy, S. Padin, T. Plagge, C. Pryke, C. L. Reichardt, J. E. Ruhl, J. T. Sayre, L. Shaw, E. Shirokoff, H. G. Spieler, Z. Staniszewski, A. A. Stark,

K. T. Story, A. van Engelen, K. Vanderlinde, J. D. Vieira, R. Williamson, and O. Zahn. A measurement of the secondary-CMB and millimeter-wave-foreground bispectrum using 800 square degrees of South Pole Telescope data. *arXiv:1303.3535*, March 2013.

[5] J. Dunkley, E. Calabrese, J. Sievers, G. E. Addison, N. Battaglia, E. S. Battistelli, J. R. Bond, S. Das, M. J. Devlin, R. Dunner, J. W. Fowler, M. Gralla, A. Hajian, M. Halpern, M. Hasselfield, A. D. Hincks, R. Hlozek, J. P. Hughes, K. D. Irwin, A. Kosowsky, T. Louis, T. A. Marriage, D. Marsden, F. Menanteau, K. Moodley, M. Niemack, M. R. Nolta, L. A. Page, B. Partridge, N. Sehgal, D. N. Spergel, S. T. Staggs, E. R. Switzer, H. Trac, and E. Wollack. The Atacama Cosmology Telescope: likelihood for small-scale CMB data. *arXiv:1301.0776*, January 2013.

[6] E. R. Fernandez, I. T. Iliev, E. Komatsu, and P. R. Shapiro. The Cosmic near Infrared Background. III. Fluctuations, Reionization, and the Effects of Minimum Mass and Self-regulation. *ApJ*, 750:20, May 2012.

[7] E. R. Fernandez, E. Komatsu, I. T. Iliev, and P. R. Shapiro. The Cosmic Near-Infrared Background. II. Fluctuations. *ApJ*, 710:1089–1110, February 2010.

[8] N. Y. Gnedin and A. H. Jaffe. Secondary Cosmic Microwave Background Anisotropies from Cosmological Reionization. *ApJ*, 551:3–14, April 2001.

[9] A. Gruzinov and W. Hu. Secondary Cosmic Microwave Background

Anisotropies in a Universe Reionized in Patches. *ApJ*, 508:435–439, December 1998.

[10] J. Harnois-Deraps, U.-L. Pen, I. T. Iliev, H. Merz, J. D. Emberson, and V. Desjacques. High Performance P3M N-body code: CUBEP3M. *arXiv:1208.5098*, August 2012.

[11] I. T. Iliev, G. Mellema, U.-L. Pen, J. R. Bond, and P. R. Shapiro. Current models of the observable consequences of cosmic reionization and their detectability. *MNRAS*, 384:863–874, March 2008.

[12] I. T. Iliev, G. Mellema, P. R. Shapiro, and U.-L. Pen. Self-regulated reionization. *MNRAS*, 376:534–548, April 2007.

[13] I. T. Iliev, G. Mellema, P. R. Shapiro, U.-L. Pen, Y. Mao, J. Koda, and K. Ahn. Can 21-cm observations discriminate between high-mass and low-mass galaxies as reionization sources? *MNRAS*, 423:2222–2253, July 2012.

[14] I. T. Iliev, U.-L. Pen, J. R. Bond, G. Mellema, and P. R. Shapiro. The Kinetic Sunyaev-Zel'dovich Effect from Radiative Transfer Simulations of Patchy Reionization. *ApJ*, 660:933–944, May 2007.

[15] I. T. Iliev and P. R. Shapiro. The post-collapse equilibrium structure of cosmological haloes in a low-density universe. *MNRAS*, 325:468–482, August 2001.

[16] A. H. Jaffe and M. Kamionkowski. Calculation of the Ostriker-Vishniac effect in cold dark matter models. *Phys. Rev.*, 58(4):043001, August 1998.

[17] E. Komatsu, J. Dunkley, M. R. Nolta, C. L. Bennett, B. Gold, G. Hinshaw, N. Jarosik, D. Larson, M. Limon, L. Page, D. N. Spergel, M. Halpern, R. S. Hill, A. Kogut, S. S. Meyer, G. S. Tucker, J. L. Weiland, E. Wollack, and E. L. Wright. Five-Year Wilkinson Microwave Anisotropy Probe Observations: Cosmological Interpretation. *ApJS*, 180:330–376, February 2009.

[18] C.-P. Ma and J. N. Fry. Nonlinear Kinetic Sunyaev-Zel'dovich Effect. *Physical Review Letters*, 88(21):211301, May 2002.

[19] M. McQuinn, S. R. Furlanetto, L. Hernquist, O. Zahn, and M. Zaldarriaga. The Kinetic Sunyaev-Zel'dovich Effect from Reionization. *ApJ*, 630:643–656, September 2005.

[20] G. Mellema, I. T. Iliev, M. A. Alvarez, and P. R. Shapiro. C^2-ray: A new method for photon-conserving transport of ionizing radiation. *New Astronomy*, 11:374–395, March 2006.

[21] A. Mesinger, M. McQuinn, and D. N. Spergel. The kinetic Sunyaev-Zel'dovich signal from inhomogeneous reionization: a parameter space study. *MNRAS*, 422:1403–1417, May 2012.

[22] H. Park, P. R. Shapiro, E. Komatsu, I. T. Iliev, K. Ahn, and G. Mellema. The Kinetic Sunyaev-Zel'dovich Effect as a Probe of the Physics of Cosmic Reionization: The Effect of Self-regulated Reionization. *ApJ*, 769:93, June 2013.

[23] A. Refregier, E. Komatsu, D. N. Spergel, and U.-L. Pen. Power spectrum of the Sunyaev-Zel'dovich effect. *Phys. Rev.*, 61(12):123001, June 2000.

[24] C. L. Reichardt, L. Shaw, O. Zahn, K. A. Aird, B. A. Benson, L. E. Bleem, J. E. Carlstrom, C. L. Chang, H. M. Cho, T. M. Crawford, A. T. Crites, T. de Haan, M. A. Dobbs, J. Dudley, E. M. George, N. W. Halverson, G. P. Holder, W. L. Holzapfel, S. Hoover, Z. Hou, J. D. Hrubes, M. Joy, R. Keisler, L. Knox, A. T. Lee, E. M. Leitch, M. Lueker, D. Luong-Van, J. J. McMahon, J. Mehl, S. S. Meyer, M. Millea, J. J. Mohr, T. E. Montroy, T. Natoli, S. Padin, T. Plagge, C. Pryke, J. E. Ruhl, K. K. Schaffer, E. Shirokoff, H. G. Spieler, Z. Staniszewski, A. A. Stark, K. Story, A. van Engelen, K. Vanderlinde, J. D. Vieira, and R. Williamson. A Measurement of Secondary Cosmic Microwave Background Anisotropies with Two Years of South Pole Telescope Observations. *ApJ*, 755:70, August 2012.

[25] R. Salvaterra, B. Ciardi, A. Ferrara, and C. Baccigalupi. Reionization history from coupled cosmic microwave background/21-cm line data. *MNRAS*, 360:1063–1068, July 2005.

[26] M. G. Santos, A. Cooray, Z. Haiman, L. Knox, and C.-P. Ma. Small-Scale Cosmic Microwave Background Temperature and Polarization Anisotropies

Due to Patchy Reionization. *ApJ*, 598:756–766, December 2003.

[27] P. R. Shapiro, M. L. Giroux, and A. Babul. Reionization in a cold dark matter universe: The feedback of galaxy formation on the intergalactic medium. *ApJ*, 427:25–50, May 1994.

[28] P. R. Shapiro, I. T. Iliev, G. Mellema, K. Ahn, Y. Mao, M. Friedrich, K. Datta, H. Park, E. Komatsu, E. Fernandez, J. Koda, M. Bovill, and U.-L. Pen. Simulating cosmic reionization and the radiation backgrounds from the epoch of reionization. In M. Umemura and K. Omukai, editors, *First Stars IV*, volume 1480 of *American Institute of Physics Conference Series*, pages 248–260, September 2012.

[29] L. D. Shaw, D. H. Rudd, and D. Nagai. Deconstructing the Kinetic SZ Power Spectrum. *ApJ*, 756:15, September 2012.

[30] R. A. Sunyaev and I. B. Zel'dovich. The velocity of clusters of galaxies relative to the microwave background - The possibility of its measurement. *MNRAS*, 190:413–420, February 1980.

[31] D. Tseliakhovich and C. Hirata. Relative velocity of dark matter and baryonic fluids and the formation of the first structures. *Phys. Rev.*, 82(8):083520, October 2010.

[32] E. T. Vishniac. Reionization and small-scale fluctuations in the microwave background. *ApJ*, 322:597–604, November 1987.

[33] S. Weinberg. *Cosmology*. Oxford University Press, Oxford, UK, 2008.

[34] O. Zahn, A. Mesinger, M. McQuinn, H. Trac, R. Cen, and L. E. Hernquist. Comparison of reionization models: radiative transfer simulations and approximate, seminumeric models. *MNRAS*, 414:727–738, June 2011.

[35] O. Zahn, C. L. Reichardt, L. Shaw, A. Lidz, K. A. Aird, B. A. Benson, L. E. Bleem, J. E. Carlstrom, C. L. Chang, H. M. Cho, T. M. Crawford, A. T. Crites, T. de Haan, M. A. Dobbs, O. Doré, J. Dudley, E. M. George, N. W. Halverson, G. P. Holder, W. L. Holzapfel, S. Hoover, Z. Hou, J. D. Hrubes, M. Joy, R. Keisler, L. Knox, A. T. Lee, E. M. Leitch, M. Lueker, D. Luong-Van, J. J. McMahon, J. Mehl, S. S. Meyer, M. Millea, J. J. Mohr, T. E. Montroy, T. Natoli, S. Padin, T. Plagge, C. Pryke, J. E. Ruhl, K. K. Schaffer, E. Shirokoff, H. G. Spieler, Z. Staniszewski, A. A. Stark, K. Story, A. van Engelen, K. Vanderlinde, J. D. Vieira, and R. Williamson. Cosmic Microwave Background Constraints on the Duration and Timing of Reionization from the South Pole Telescope. *ApJ*, 756:65, September 2012.

[36] O. Zahn, M. Zaldarriaga, L. Hernquist, and M. McQuinn. The Influence of Nonuniform Reionization on the CMB. *ApJ*, 630:657–666, September 2005.

[37] Y. B. Zel'dovich and R. A. Sunyaev. The Interaction of Matter and Radiation in a Hot-Model Universe. *AP&SS*, 4:301–316, July 1969.